ADVANCED FUNCTIONAL MATERIALS
www.afm-journal.de

Temperature-Resilient Polymeric Memristors for Effective Deblurring in Static and Dynamic Imaging

Ziyu Lv, Ming-Hao Jiang, Hui-Ying Liu, Qing-Xiu Li, Tao Xie, Jingya Yang, Yan Wang, Yongbiao Zhai, Guanglong Ding, Shirui Zhu, Jia-Hua Li, Miao Zhang, Ye Zhou, Bobo Tian, Wai-Yeung Wong,* and Su-Ting Han**

Organic memristors have emerged as promising candidates for neuromorphic computing due to their potential for low-cost fabrication, large-scale integration, and biomimetic functionality. However, their practical applications are often hindered by limited thermal stability and device-to-device variability. Here, an organic polymer-based memristor using a thiadiazolobenzotriazole (TBZ) and 2,5-Dioctyl-3,6-di(thiophen-2-yl)pyrrolo[3,4-c]pyrrole-1,4(2H,5H)-dione (DPP)-based conjugated polymer is presented that exhibits exceptional thermal stability and reliable resistance switching behavior over a wide temperature range (153–573 K). The device leverages a charge-transfer mechanism to achieve gradual and uniform resistance switching, overcoming the challenges associated with filamentary-based mechanisms. The memristor's exceptional thermal stability and consistent performance enable its integration into various applications, including image processing. The device's ability is demonstrated to effectively deblur images, even under varying temperature conditions, showcasing its potential for robust and reliable neuromorphic computing. This study establishes a pathway toward high-performance, thermally stable organic memristors for advanced neuromorphic computing and artificial intelligence applications.

1. Introduction

The pursuit of electronic systems with cognitive, decision-making, and interactive capabilities has driven significant advancements in artificial intelligence.[1–6] This endeavor has also catalyzed the development of advanced functional materials and devices optimized for information storage and processing.[7–15] A pivotal milestone in this field was the landmark study of Williams and Strukov in 2008, which spurred the rapid evolution of memristor technology.[16] Memristors, with their ability to modulate resistance based on the history of electrical bias, along with high data density, reliability, low power consumption, fast switching speeds, and a compact footprint, offer a compelling alternative to conventional charge-based memory technologies.[11,17–21] In addition, memristors enable intrinsic information processing through "compute-in-physics," utilizing physical phenomena to carry out complex signal transformations.

Z. Lv, M.-H. Jiang, J. Yang, Y. Zhai, G. Ding
College of Electronics and Information Engineering
Shenzhen University
Shenzhen 518060, P. R. China

H.-Y. Liu, S. Zhu, M. Zhang, W.-Y. Wong, S.-T. Han
Department of Applied Biology and Chemical Technology and Research Institute for Smart Energy
The Hong Kong Polytechnic University
Hung Hom, Hong Kong 000000, P. R. China
E-mail: bjtumiao.zhang@polyu.edu.hk; wai-yeung.wong@polyu.edu.hk; suting.han@polyu.edu.hk

The ORCID identification number(s) for the author(s) of this article can be found under https://doi.org/10.1002/adfm.202424382

DOI: 10.1002/adfm.202424382

Q.-X. Li, T. Xie
Institute of Microscale Optoelectronics
Shenzhen University
Shenzhen 518060, P. R. China

Y. Wang
School of Microelectronics
Hefei University of Technology
Hefei 230009, P. R. China

J.-H. Li
The Hong Kong Polytechnic University Shenzhen Research Institute
Shenzhen 518060, P. R. China

Y. Zhou
Institute for Advanced Study
Shenzhen University
Shenzhen 518060, P. R. China

B. Tian
Key Laboratory of Polar Materials and Devices
Ministry of Education
East China Normal University
Shanghai 200241, P. R. China

This capability significantly enhances both area and energy efficiency, positioning memristors as promising candidates for applications in neuromorphic chips, artificial intelligence, and in-sensor computing.[20,22–26] Regarding material selection, a diverse range of materials—encompassing inorganic oxides,[27,28] low-dimensional systems,[18,29–32] phase-change materials,[33,34] organic compounds[35] and heterojunction materials[36–38]—has been investigated for memristor development. Among these, oxide-based devices have proven to be particularly promising due to their considerable application potential.[39–46] However, challenges such as elevated forming voltages and currents, significant set/reset voltages, as well as spatial and temporal non-uniformity, hence hindering the advancement of high-density memory technologies.[47–50]

Among other genres, organic memristors garnered considerable interest from the research community. This is due to their inherent nanometer-scale material properties and their versatile ionic-electronic behaviors, which offer significant advantages for data storage and processing. Additionally, their solution processability facilitates cost-effective manufacturing, while their chemically tunable functionalities further enhance their attractiveness.[51–54] To fabricate high-performance memristors and neuromorphic chips, considerable effort has been devoted to developing organic memristors with diverse resistance-switching mechanisms—including redox processes,[55–58] molecular conformation reconstruction,[59] ion migration,[60,61] and charge transfer[62,63]—that enable precise modulation of electronic and electrical states within organic molecules. Recent pioneering studies, for example, showcase the development of a metal-organic complex with five distinct redox states to create a molecular memristor capable of performing advanced conditional logic and highlight the advancement of an organic macromolecule with enhanced ion-molecule interactions and precise structural ordering, thus achieving exceptional device miniaturization (50×50 nm^2) and remarkable uniformity, with conductance variation minimized to just 0.29%.[64] Despite significant research investment, the commercial translation of organic memristors remains unachieved, with key performance aspects, such as device stability and endurance, still requiring improvement.[65–67] For instance, organic memristors are often hindered by inadequate thermal stability, which poses a substantial challenge to maintaining optimal device functionality. Robust thermal resilience is paramount for the integration of these memristors as artificial synaptic/neuronic elements in neuromorphic systems, particularly when intended for deployment in extreme environments, such as aerospace (i.e., space exploration), energy (i.e., geothermal energy), and military applications (hypersonic vehicles). Despite the critical nature of thermal stability, few investigations have thoroughly examined this characteristic in organic memristors. Furthermore, the operational temperature ranges reported thus far fall short of meeting the stringent requirements for advanced applications, particularly in the aerospace and military sectors.

In this study, we propose an organic polymeric memristor based on acceptor-acceptor (2,5-dioctyl-3,6-di(thiophen-2-yl) pyrrolo[3,4-c]pyrrole-1,4(2H,5H)-dione (DPP) acts as the acceptor 1; thiadiazolobenzotriazole (TBZ) acts as the acceptor 2) conjugated polymer-(PTBZ-DPP) capable of operation under a wide temperature range (153–573 K, thermal treatment) and forming-free switching behavior with good uniformity. The polymer-based memristor in PTBZ-DPP, constructed with two strong electron-withdrawing units to facilitate intramolecular charge transfer (ICT), achieves gradual resistance switching. Under electrical stimulation, the stable charge transfer process in the device effectively regulates charge transport within the polymer film, resulting in a reliable gradual memristive response. In contrast, filamentary memristors, while the most widely studied and exhibiting excellent performance characteristics, face challenges such as stochastic ion migration leading to poor device uniformity and difficulties in constructing prototypes with a wide operational range. In our study, the charge transfer mechanism inherently avoids problems associated with the overgrowth or random formation of conductive filaments. The charge transfer process utilized in this system ensures superior spatiotemporal consistency, with low operational voltage variations, and multi-bit storage capabilities. Moreover, the polymer system exhibits excellent thermal tolerance and environmental stability, with its memristive properties remaining virtually unaffected after both low- and high-temperature treatments. Collectively, the charge transfer-based memristor in our study synchronously improves device uniformity and expands the operational temperature range, making it highly suitable for specialized application scenarios. Thanks to its good stability and consistent resistance switching behavior, this memristor is well-suited for applications such as blurred image recognition and motion deblurring. For example, in the blurred image recognition task, the memristor array maintains robust image processing capabilities across different temperatures, enhancing recognition accuracy by over 30% compared to untreated blurred images, further demonstrating the device's thermal robustness.

2. Results and Discussion

2.1. Organic Memristors and Their Switching Behaviors

Detailed synthetic procedures for the polymer are available in Figure S1 (Supporting Information). The PTBZ-DPP thin film described herein was deposited onto a pre-patterned ITO glass substrate via spin coating. The choice of Au as the top electrode material is based on its inert nature. Our fundamental device architecture and cross-sectional scanning electron microscopy (SEM) image, illustrated in **Figure** 1a,b, feature a PTBZ-DPP layer sandwiched between Au and ITO electrodes. The thickness of the switching material is ≈130 nm. Comprehensive details of the device fabrication process are outlined in the Experimental Section and Figure S2 (Supporting Information). Figure 1c presents the chemical structures of two acceptors, TBZ and DPP(containing -Sn end group), serve as monomers for polymerization. Figure 1d shows the typical *I–V* curves of the PTBZ-DPP memristor under successive 10 cycles of positive and negative voltage sweeps at room temperature. The memristor shows pinched hysteresis loops upon bipolar periodic intuitive illustration of the evolution of peak current with the voltage sweep cycle (Figure 1e,f). For instance, the peak current increases gradually from 0.2 mA to over 0.4 mA, whereas negative current sweeps lead to a gradual recovery of the current to its initial value. Increasing the molecular weight can negatively impact the solubility and uniform distribution of polymer molecules in the

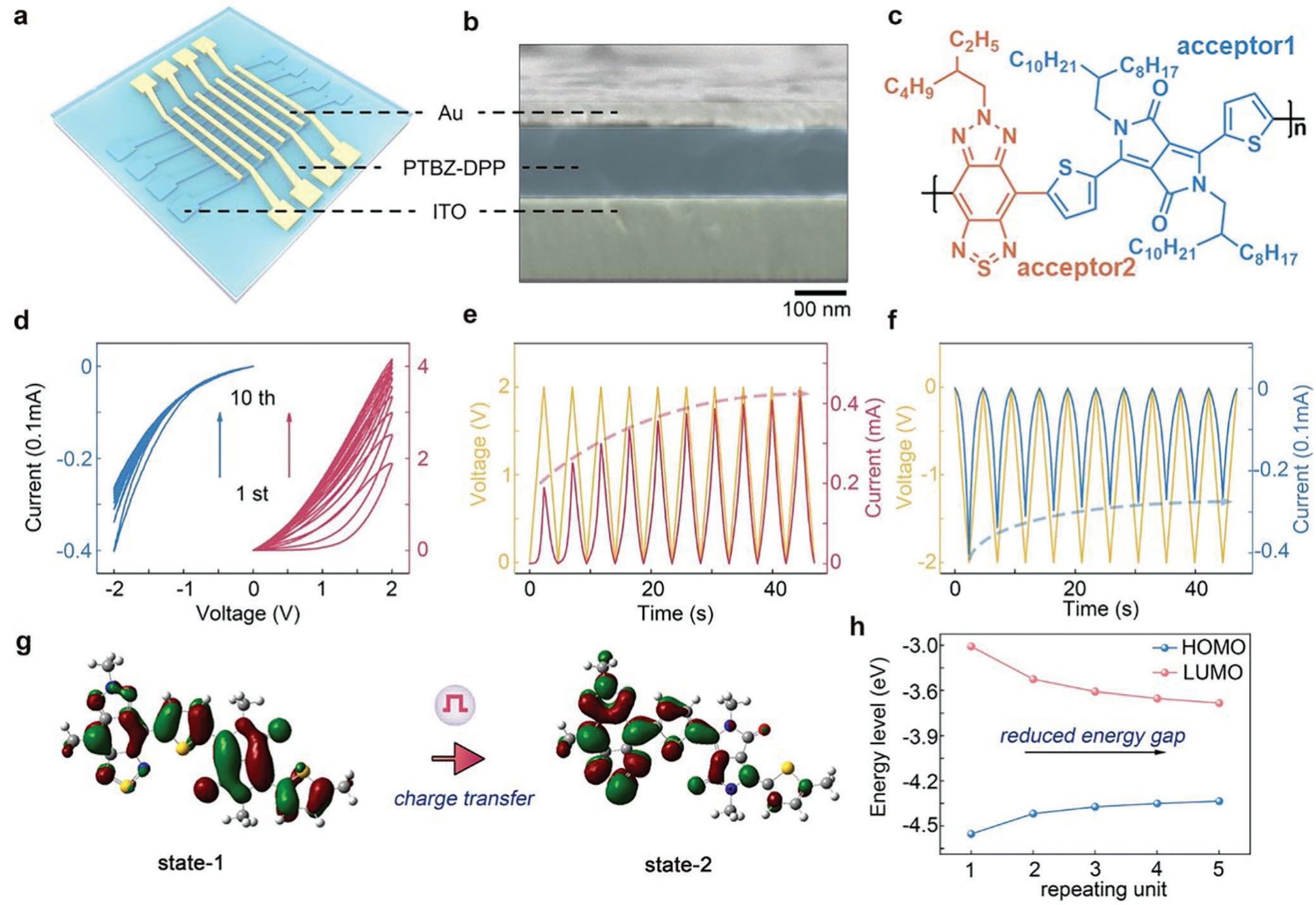

Figure 1. Schematic and characterization of the PTBZ-DPP-based memristor. a) Schematic and b) cross-section SEM image of the polymeric memristor in this study, with PTBZ-DPP as the switching material, scale bar: 100 nm; c) Molecular view of the TBZ-DPP; d) *I–V* characteristics of PTBZ-DPP-based memristor under successive positive (red) and negative (blue) voltage sweeps. e,f) *I–t* characteristics of PTBZ-DPP-based memristor under successive e) positive and f) negative voltage sweeps (0 → 2(-2) → 0), extracted from (d), step: 0.02 V. g) Schematic illustration of ICT induced molecular state change (one repeating unit). h) Energy level variations as a function of the number of repeating unit.

solvent, leading to non-uniformity in the resulting film. This often results in significant fluctuations in the memristor curves, and in some cases, the memristive effect may become unobservable (Figures S3–S5, Supporting Information). Decreasing the thickness of the PTBZ-DPP film can cause to a reduction or even elimination of hysteresis, as shown in Figures S5 and S6 (Supporting Information). The PTBZ-DPP introduces two acceptors with different electron-withdrawing capability, facilitating intramolecular charge transfer under electrical stimulation and consequently inducing changes in the molecular dipole moment (Figure S7, Supporting Information). By examining an individual repeating unit using DFT calculation, we observe that electrical excitation triggers charge transfer within the molecule, leading to enhanced electron mobility and conductivity (Figure 1g and Figure S8, Supporting Information). The use of inert electrodes in our device eliminates the possibility of conductive filament formation as the mechanism for resistive switching. Instead, we attribute the observed resistive switching to intramolecular charge transfer, consistent with findings reported in previous studies.[68] Moreover, as the molecular weight increases (i.e., the number of repeating unit), the energy bandgap narrows (Figure 1h). A higher number of repeating unit implies a greater number of potential charge transfer pathway within the molecule.

2.2. Temperature and Environmental Stability

Subsequently, we evaluated the stability of the memristor under various thermal and environmental conditions. First, the devices were subjected to different temperatures (153, 373, 473, and 573 K) for 30 min, followed by memristive performance testing (**Figure 2a**). We observed that under 20 voltage pulses, the devices exhibited highly consistent memristive behavior, demonstrating good high-temperature tolerance and potential for applications under extreme conditions. The surface roughness of PTBZ-DPP films treated at different temperatures was also characterized. AFM images revealed no significant changes in film morphology or roughness after either low or high-temperature treatments, indicating excellent thermal stability of the polymer film (Figure 2b). A comparative graph of peak currents under pulse stimulation further confirmed the temperature robustness

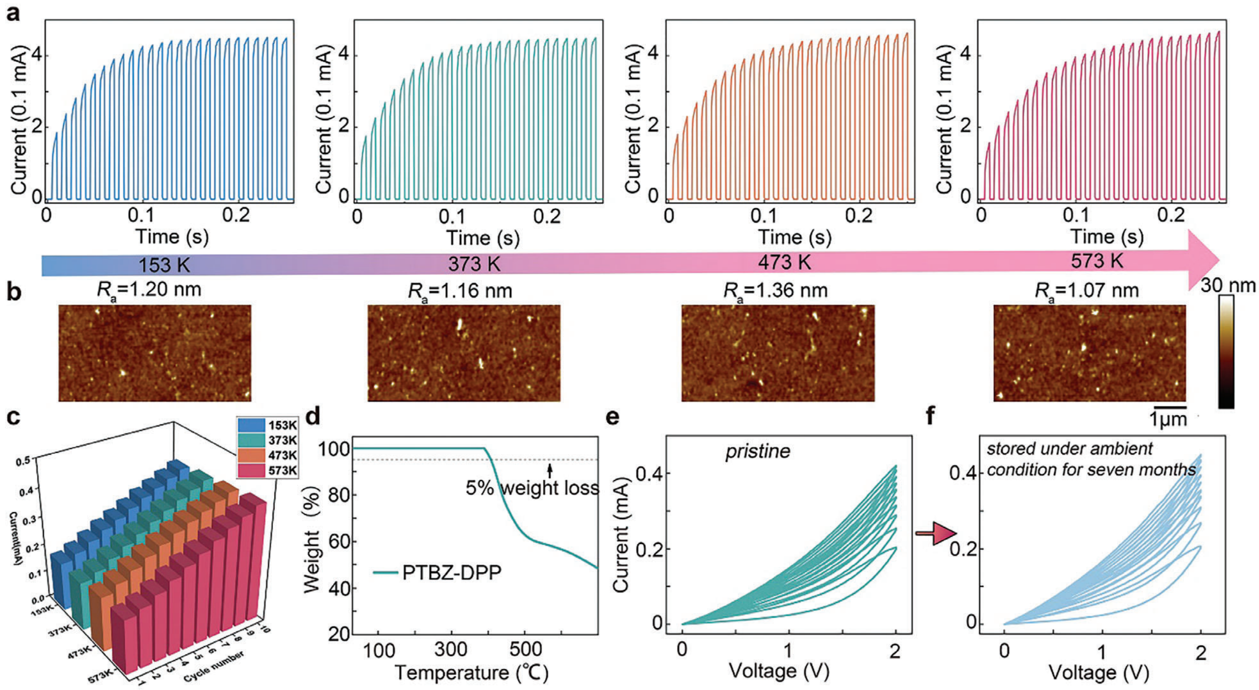

Figure 2. Temperature and environmental stability tests of the PTBZ-DPP-based memristor. a) Conductance response induced by successive voltage pulses (V_{pulse} = 3 V, duration 1 ms) of PTBZ-DPP-based memristor and b) corresponding AFM topography images of the PTBZ-DPP film, treated at different temperatures (153 K, 373 K, 473K and 573K). All devices or films were conditioned at different temperatures for one hour before being tested at room temperature. c) Histogram of the peak currents of PTBZ-DPP-based memristor induced by successive voltage pulses, at different temperatures (153 K, 373 K, 473K and 573K). d) thermogravimetric analysis (TGA) of the PTBZ-DPP film. *I–V* characteristics of e) PTBZ-DPP-based memristor at pristine state, and f) stored under ambient condition for seven months.

of the devices after different thermal treatments (Figure 2c). Thermogravimetric analysis showed that the polymer material exhibits good thermal responsiveness, with only a 5% mass loss at 681 K (Figure 2d). Additionally, the memristive effect of the devices remained nearly unchanged after being stored in a normal environment (at room temperature in air, without any specific protection from light exposure) for seven months, further proving the excellent environmental stability of the devices (Figure 2e,f).

2.3. Neuromorphic Behavior

In addition, the charge transfer behavior between acceptor 1 and acceptor 2 within the PTBZ-DPP film can be employed to simulate neurotransmitter transmission in biological synapses (**Figure 3a**). The charge transfer behavior induces the formation and disruption of conductive pathways within the dielectric layer. With increased voltage stimuli, these pathways demonstrate prolonged relaxation or retention times. As a result, the steady-state evolution of these conductive pathways can be harnessed to simulate synaptic plasticity. Long-term plasticity, encompassing both long-term potentiation (LTP) and long-term depression (LTD), is essential for memory-related and learning-related behaviors. Based on the multibit storage characteristics of the memristor, LTP and LTD are simulated through continuous positive and negative pulse stimuli. As shown in Figure 3b, 40 continuous positive and negative voltage stimuli gradually increase or decrease the conductance state, with blue and red dots representing synaptic current changes in LTP and LTD, respectively. The device exhibits excellent LTP and LTD performance, with linearity coefficients of 0.937 and -1.172 for LTP and LTD, respectively. The polymer memristor in this study uses a charge transfer mechanism that induces gradual resistive switching under electrical stimulation. The conductance changes are linear with the number of voltage pulses, as opposed to abrupt jumps in filamentary memristors, enabling precise and progressive tuning of synaptic weights. This symmetrical and linear conductance modulation is advantageous for enabling brain-inspired hardware with "blind" synaptic weight update capability. After exposure to both low and high-temperature treatments, the memristor exhibits similar synaptic plasticity, indicating its excellent thermal stability (Figure S9, Supporting Information). As shown in Figure 3c, under 400 pulses (alternating between 20 positive and 20 negative pulses), the synaptic weight updates exhibit excellent symmetry and reproducibility. Additionally, this gradual rise and fall of current responses offer a fundamental framework for modeling the complex interplay of excitation and inhibition in biological synapses. Paired-pulse facilitation (PPF) and paired-pulse depression (PPD) are forms of short-term synaptic plasticity mechanisms that play critical roles in shaping neuronal responses to rapidly occurring spike trains. PPF enhances the response to a second spike, while PPD suppresses it, thereby enabling the fine-tuning of synaptic transmission. By adjusting the interval between pulses, the memristor can also emulate PPF and PPD phenomena. As depicted

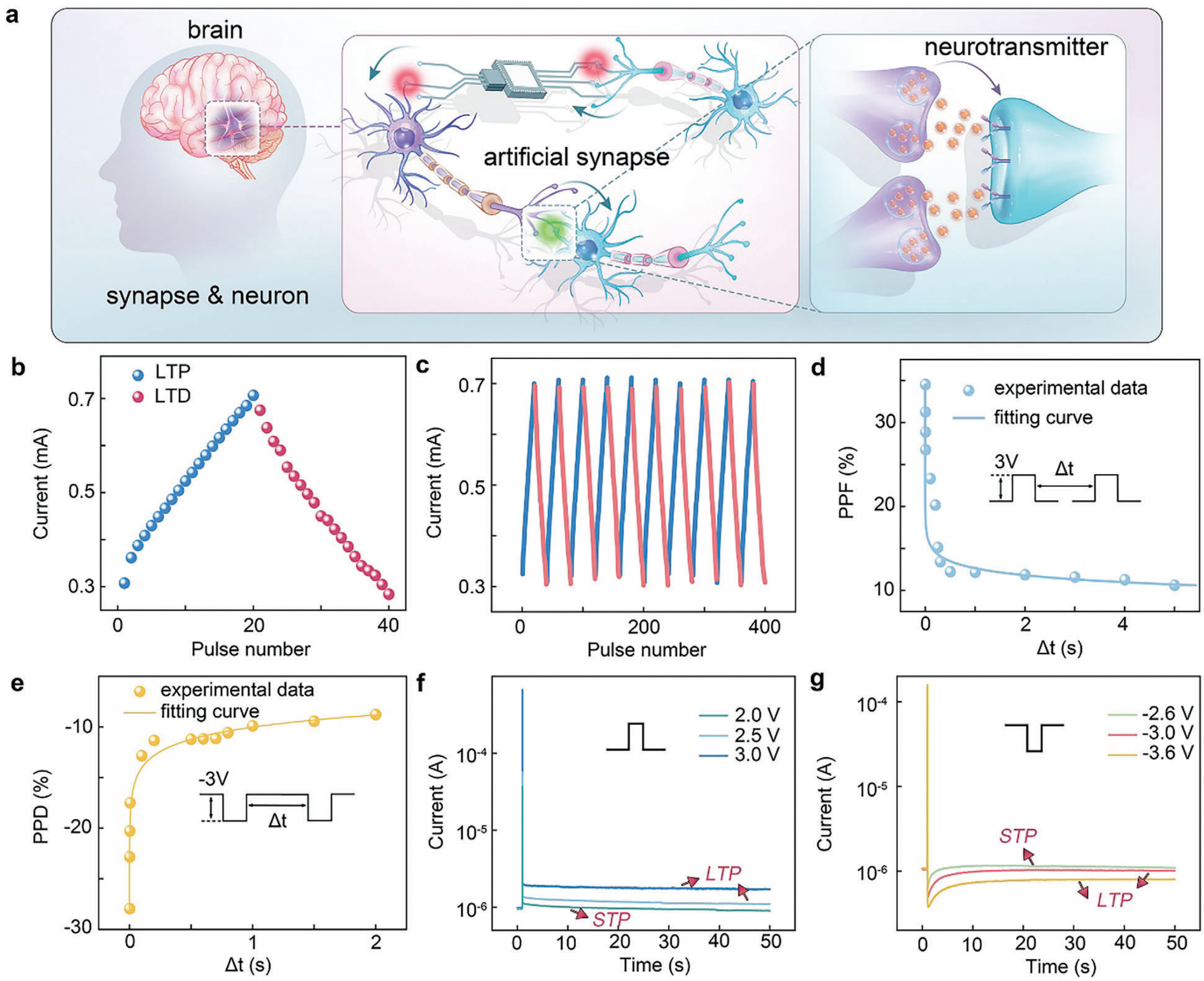

Figure 3. Neuromorphic behavior. a) Schematics illustration of a biological synapse, and its electronic counterpart. b) Long-term potentiation (LTP) and depression (LTD) displaying 20 discrete conductance states when the memristor is controlled with input pulses (3.0 V, -4.2 V duration, 5 ms). c) Synaptic weight updates were induced by a 400 pulse protocol consisting of alternating 20 positive and 20 negative pulses. Experimental demonstration of d) paired-pulse facilitation (PPF) and e) paired-pulse depression (PPD) in the PTBZ-DPP-based memristor. Postsynaptic currents evoked by varying amplitudes of positive (f: 2.0 V, 2.5 V and 3.0 V) and negative voltage pulses (g: -2.6 V, -3.0 V and -3.6 V).

in Figure 3d,e, the PPF and PPD phenomena were simulated by applying two consecutive voltage pulses of the same polarity (3 V, 5 ms) and opposite polarity (−4.2 V, 5 ms), respectively. The observed PPF can be attributed to the temporal summation of neurotransmitter release. When the second stimulus arrives at the presynaptic terminal, residual neurotransmitter from the first stimulus remains in the synaptic cleft, leading to an enhanced postsynaptic response. Consequently, PPF is directly correlated with the inter-stimulus interval. We investigated the PPF synaptic function index in our basic memristor using the following equation:

$$\mathrm{PPF} = \frac{A_2 - A_1}{A_1} \times 100\% \tag{1}$$

where A_1 and A_2 denote the current amplitudes measured in response to the initial and subsequent 3 V positive stimuli. Figure 3d illustrates a significant decrease in PPF increment with increasing pulse intervals. Moreover, we can flexibly switch between short-term and long-term plasticity by modulating the pulse amplitude. As shown in Figure 3f,g, with lower voltage amplitude stimulation (2.0 V, -2.6 V), the post-synaptic current recovers to its initial state within a few seconds; increasing the voltage amplitude (2.5 V and 3.0 V, -3.0 V and -3.6 V) significantly prolongs the retention time of the post-synaptic current, enabling the simulation of long-term plasticity.

2.4. Dynamic Response of the Memristors

Subsequently, the dynamic response of the memristors was comprehensively examined using sequences of voltage stimuli with varied frequencies, durations and pulse amplitudes. To investigate the effect of stimulation frequency on the dynamic response of the memristors, we first kept the input voltage duration and amplitude constant. As shown in **Figure 4a**, under

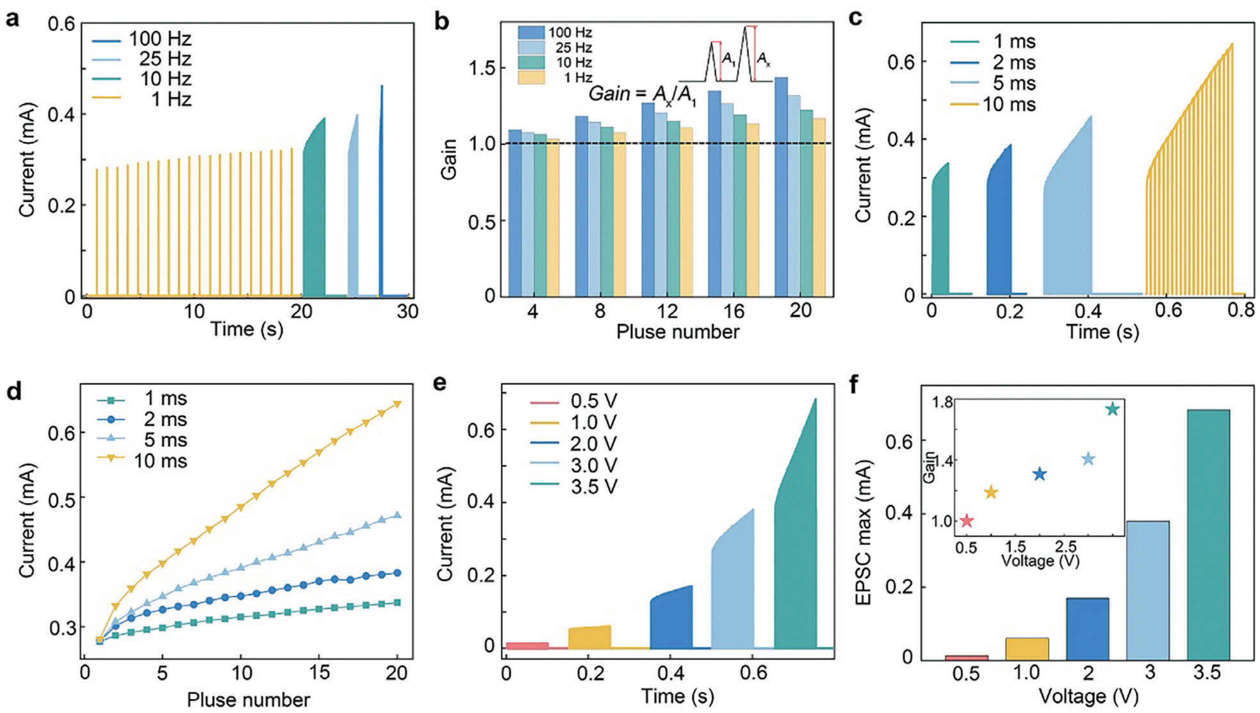

Figure 4. a) Current response measured during the application of 20 input pulses at varying frequencies (1, 10, 25, and 100 Hz). b) Variation in peak current with pulse number, derived from (a); the conductance gain is defined as the ratio A_x/A_1. c) Current response recorded during the application of 20 input pulses with different durations (1, 2, 5, and 10 ms). d) Variation in peak current with pulse number, derived from (c). e) Current response measured during the application of 20 input pulses at different amplitudes (0.5, 1.0, 2.0, 3.0, and 3.5 V). f) Peak current induced by the 20-th input pulse, derived from (e). Inset: Variation in conductance gain with pulse number.

a 1 Hz voltage stimulus, the peak current of the device gradually increases with the number of pulse, similar to the synaptic behavior observed in our previous studies. With higher stimulation frequencies (10 Hz, 25 Hz, and 100 Hz), the rate of current increase accelerates, allowing higher currents to be achieved after 20 pulses. We define the current gain as A_x/A_1, where A_x represents the peak current of the x-th voltage pulse. As illustrated in Figure 4b, higher frequency stimuli result in greater current gains, with a gain of approximately 1.4 observed at 100 Hz. Specifically, at low temperature, and high temperature, the current gain shows similar behavior, underscoring the device's reliable performance across a broad temperature range (Figure S10, Supporting Information). The increase in current gain with higher frequency can be attributed to the relaxation time required for the device to return to its initial state after each voltage stimulus. As the input frequency increases, the influence of each preceding pulse on the subsequent one becomes more pronounced, resulting in a significant enhancement in the peak current. In addition to pulse frequency, significant current gain can also be achieved by extending the pulse duration. As shown in Figure 4c,d, when the pulse width is increased from 1 to 10 ms, the peak current at the 20-th pulse rises from 0.34 to 0.64 mA, with the current gain increasing from 121% to 228%. Furthermore, we observed a strong linear relationship between the peak current and the number of pulse from the third pulse onwards, demonstrating potential for "blind" synaptic weight updating. Due to the threshold switching characteristics of memristors, the amplitude of the input voltage has a pronounced effect on their dynamic response. When the input voltage pulses are below or near the threshold, the device exhibits little to no peak current gain, as depicted in Figure 4e. However, as the voltage increases, additional input pulses lead to a significant rise in current. At a pulse voltage of 2.5 V, the peak current at the 20-th pulse reaches approximately 0.7 mA, with a gain approaching 1.8 (Figure 4f). In addition to achieving various current gains through the methods described above, our memristors can also exhibit distinguishable, multilevel conductance states within voltage pulse sequences, which is critical for neuromorphic applications such as reservoir computing.[69–71] Our experimental results show that, under a sequence of four pulse trains (3 V, 100 Hz, 5 ms), our device can achieve at least sixteen distinct and highly distinguishable resistance levels. Within a wide temperature range (153–573 K), the memristor can maintain distinguishable multi-level conductance states, as shown in Figure S11 (Supporting Information). Multilevel conductance and dynamic response of the polymer memristor enable efficient data storage, time-dependent processing, and are ideal for reservoir computing tasks like pattern recognition, and predictive modeling.

2.5. Memristor-Assisted Blurred Image Recognition Task

The presence of noise significantly degrades image quality and impedes effective information transmission. In the realm of artificial intelligence, models are generally trained on datasets characterized by clear, distinct features and minimal disturbances.

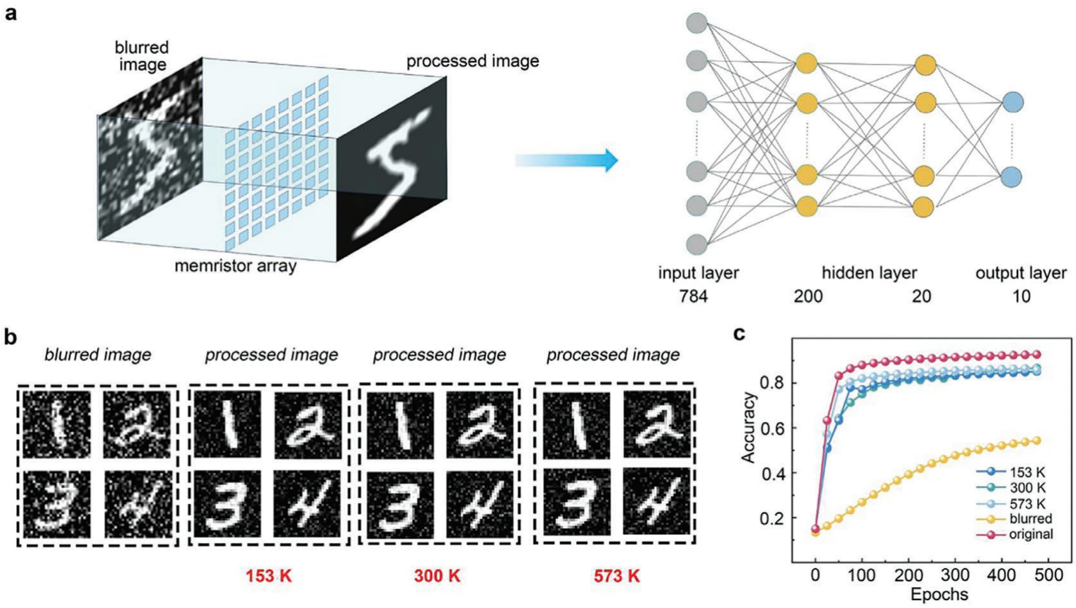

Figure 5. Simulations of blurred image recognition in a neuromorphic system utilizing PTBZ-DPP-based memristors. a) Schematic representation of a neuromorphic system leveraging a memristor array for image deblurring, integrated with an artificial neural network for subsequent image recognition. b) Examples depicting blurred images (left) and the corresponding images after memristor-based pre-processing. The memristor was subjected to temperature treatments at 153, 300, and 573 K. c) Comparative analysis of image recognition rates for the original, blurred, and processed images (The memristor was subjected to temperature treatments at 153, 300, and 573 K).

Consequently, their performance is often substantially compromised when exposed to noisy input data, leading to reduced accuracy in recognition and prediction tasks. The introduction of noise (blurred image) not only diminishes the values of key feature pixels but also introduces non-zero values to originally zero pixels, thereby complicating the prediction process. Thus, the challenge in image denoising is to effectively preserve critical feature information while eliminating noise. In this study, we first employ the threshold-switching properties of memristors to denoise blurred images. Subsequently, we utilize artificial neural networks to analyze the processed images, as depicted in **Figure** 5a. Figure 5a demonstrates the image deblurring performance of the memristor array (Figure S12 in the Supporting Information). The array processes images containing "5" body patterns against a noisy background. Brighter pixels, representing the body patterns, are represented by intense electrical input with a 3 V pulse amplitude, while the background pixels are simulated with weaker electrical input at a 0.5 V voltage pulse. The blurred images display a contrast ratio of 6 between the body patterns and the background noise. The images are consecutively input into the memristor array, which is emulated by continuously applied pulse input ($N = 20$). Due to the memristor's threshold-switching characteristics, it remains predominantly in the high-resistance state (HRS) with minimal current (0.53 μA) when subjected to 0.5 V pulse input (corresponding to the background pixels). In contrast, under 3 V pulse input (corresponding to the body pattern pixels), it produces progressively higher currents (680 μA). The output signals from the memristors in the array are represented by the spiking currents recorded after the 20-th input pulse. The contrast between the body pattern and background noise in the output is significantly enhanced compared to the input blurred image. As a result, the background noise is effectively filtered, allowing for a much clearer delineation of the body pattern. As illustrated in Figure 5b, the delineation of the digits "1," "2," "3," and "4" is significantly sharper after denoising with the memristor array, which was subjected to different temperature treatments of 153, 300, and 573 K, respectively. To recognize handwritten digits in the 28×28 pixel images, we developed a four-layer neural network architecture consisting of 784 input nodes, two hidden layers with 200 and 20 nodes, and an output layer comprising 10 nodes. Figure 5c illustrates the accuracy during the recognition process for original, blurred, and processed images. After 500 epochs, the neural network attains a recognition accuracy of 92.78% for the original images. In contrast, for blurred images, the network's accuracy is markedly lower, reaching just 54.37%. However, when the images are denoised using the proposed system, the recognition accuracy improves significantly, surpassing 85% after 500 epochs. These results demonstrate that the image deblurring process using the memristor can effectively enhance the image recognition accuracy. Moreover, under different temperature treatments (153, 300, and 573 K), the system consistently achieves high recognition accuracy, with all conditions maintaining performance above 85%, highlighting the robustness of the memristor-based approach across a broad temperature range.

2.6. Memristor-Assisted Motion Deblurring of License Plates

Beyond static deblurring, we further investigated the performance of the memristor in dynamic tasks. The motion deblurring task plays a pivotal role in enhancing image recognition

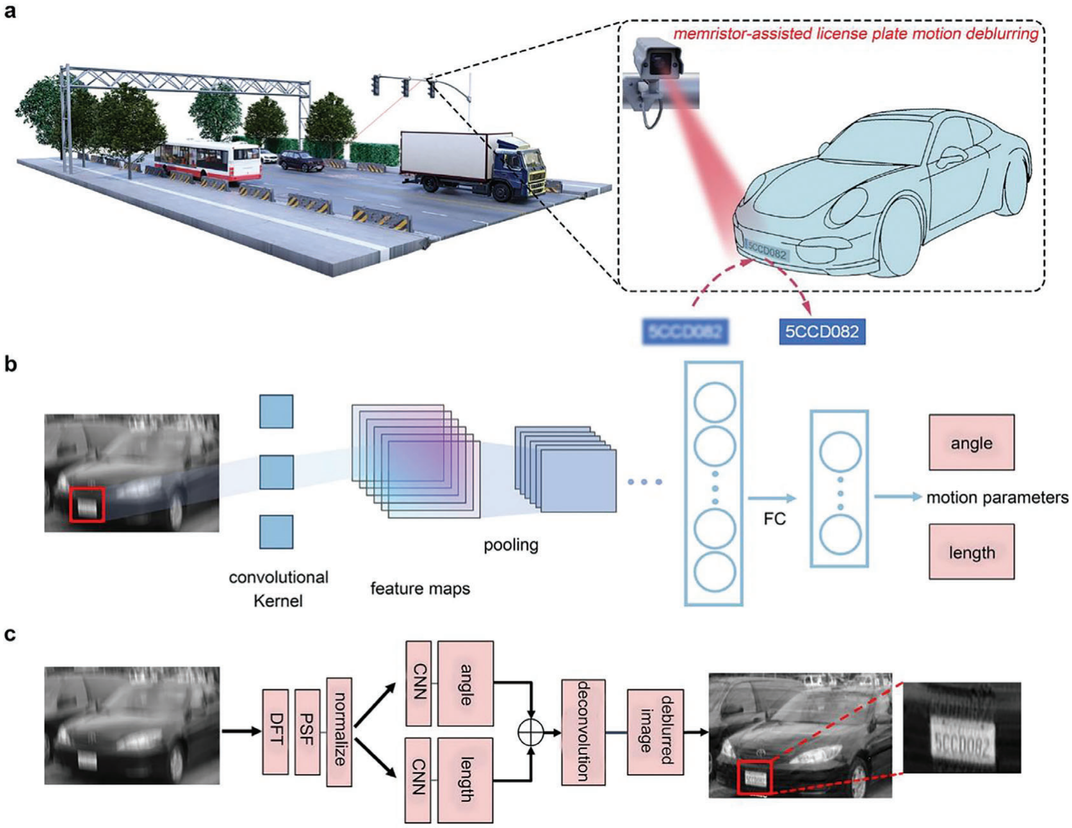

Figure 6. a) Schematic illustration of a license plate motion deblurring task facilitated by memristive hardware. b) Diagram of the CNN architecture used to identify motion parameters, including angle and length. c) Schematic depiction of the memristor-assisted CNN deblurring process and its resulting deblurred image.

performance, as blurred images can significantly degrade the accuracy of neural networks. Effective deblurring techniques restore image clarity, enabling more precise feature extraction and improved classification outcomes, which are critical for various applications in computer vision and artificial intelligence. The capabilities of image processing for license plate motion deblurring are further illustrated through the use of the proposed PTBZ-DPP-based memristors (**Figure 6a**). The blind deconvolution algorithm is the most widely used method for tackling image deblurring. This approach necessitates the estimation of blur kernel parameters, such as the length and orientation, which are crucial for correcting image distortion. Manually inputting parameters is a tedious trial-and-error process. To address this issue, we developed a convolutional neural network (CNN) that leverages the memristor's LTP/LTD characteristics (Figure 3b) to update weights and optimize the model. The CNN was optimized to derive an optimal model through iterative updates of synaptic weights in the spiking mode. This optimization process is facilitated by the implementation of both long-term potentiation (LTP) and long-term depression (LTD) mechanisms. The nonlinear current-voltage characteristic of the device was well-described by the following equations:

$$I_{n+1} = I_n + \Delta I_p = I_n + \alpha_p \exp\left[\kappa_d \left(G_{\min} - G_n\right) / \left(G_{\max} - G_{\min}\right)\right] \tag{2}$$

$$I_{n+1} = I_n + \Delta I_d = I_n + \alpha_d \exp\left[\kappa_d \left(G_n - G_{\max}\right) / \left(G_{\max} - G_{\min}\right)\right] \tag{3}$$

where α represents the change in conductance and k quantifies the degree of nonlinearity. The blurred image is fed into the model, where multiple convolutional and pooling layers extract features, ultimately producing the blur kernel parameters (length and angle) through the fully connected layer (Figure 6b and Figure S13, Supporting Information). Once the blur kernel parameters are obtained, deconvolution can be applied to the image using a deblurring algorithm. As shown in Figure 6c, the blurred car image becomes noticeably clearer after deblurring. Previously illegible details, such as the license plate number (i.e., 5CCD082), become distinguishable.

3. Conclusion

In this study, we developed and characterized PTBZ-DPP-based organic memristors, demonstrating their potential for neuromorphic and image-processing applications. The memristors exhibit reliable analog switching behavior with pinched hysteresis loops, arising from intramolecular charge transfer between two acceptor units. This mechanism is further supported by the device's molecular design, which facilitates increased conductivity under electrical stimulation, without the

ADVANCED FUNCTIONAL MATERIALS
www.afm-journal.de

formation of conductive pathways. Our findings also reveal that the memristors exhibit excellent thermal stability, maintaining performance across a wide temperature range, and remarkable environmental robustness, with memristive properties preserved after prolonged storage. In terms of neuromorphic behavior, the PTBZ-DPP memristors successfully emulate synaptic plasticity mechanisms such as long-term potentiation (LTP) and depression (LTD), paired-pulse facilitation (PPF) and depression (PPD), through controlled voltage stimuli. These characteristics provide a foundation for the development of brain-inspired hardware capable of dynamic synaptic weight updates, essential for in-memory computing tasks. Beyond neuromorphic functions, the memristors also demonstrate promising capabilities in image processing, particularly in image denoising and deblurring tasks. We demonstrated that the threshold-switching characteristics of the memristor enable effective noise filtering, significantly enhancing the clarity of blurred images. This approach improves the accuracy of neural network-based image recognition, as evidenced by improved performance in handwritten digit recognition tasks. Additionally, the memristor's LTP/LTD characteristics were employed in a convolutional neural network (CNN) for motion deblurring of license plate images, achieving successful restoration of image clarity and readability. The precise regulation of charge transfer in PTBZ-DPP memristors is crucial for building high-performance neuromorphic hardware. Two strategies could be explored to enhance this system. First, optimizing molecular design to enable multilevel electrically-driven charge transfer processes could allow for the construction of neuromorphic hardware with higher storage density. Second, through chemical modification, charge transfer driven by other external fields—such as light-driven processes—can be realized. This would endow the device with multimodal programming capabilities, advancing its application in areas like in-sensor computing and beyond.

4. Experimental Section

Device Fabrication: The initial patterned ITO glass substrate (2 cm × 2 cm) was thoroughly cleaned using sequential ultrasonication in deionized water and ethanol for 15 min each, followed by UV-ozone treatment to remove organic residues and improve surface wettability. A PTBZ-DPP solution with a concentration of 15 mg mL^{-1} in o-dichlorobenzene was prepared for subsequent spin coating. The cleaned ITO substrate was mounted in a spin coater, where vacuum suction was applied to secure it. A measured quantity of the polymer solution was dispensed onto the substrate, and spin coating was initiated with a two-step process: first at 500 rpm for 5 seconds, followed by 1000 rpm for 40 s to achieve a uniform film. For post-deposition, the sample was annealed at 150 °C for 1 h under a nitrogen atmosphere to improve film stability and morphology. Finally, an Au top electrode was deposited onto the active layer using vacuum thermal evaporation through a shadow mask, maintaining a chamber pressure of 4.0×10^{-4} Pa.

Electrical Measurements: The electrical characteristics of PTBZ-DPP-based memristors were systematically evaluated using a Keithley 4200 parameter analyzer in the voltage-sweep mode, with a current compliance of 1.0 mA implemented to safeguard the device from permanent damage. For dynamic pulse measurements, a Keysight B2902A source meter was employed to generate precise input pulses, while output characteristics were continuously monitored in real-time to capture transient switching behavior accurately.

Simulations of Blurred Image Recognition: To assess the denoising capability of the memristor, Gaussian white noise was randomly applied to images from the original dataset using MATLAB to generate noisy samples. The memristor's denoising effect was then simulated in Python, after which the processed results were input into an artificial neural network (ANN) to evaluate and compare the training performance.

Memristor-Assisted Motion Deblurring: When a camera captures a moving object, relative motion results in image blurring, which can be represented as a convolution of the original image with a motion blur kernel. Restoring such images requires accurate estimation of the blur direction and length. In this study, this challenge is addressed using a convolutional neural network (CNN) implemented in Python, which leverages the memristor's LTP/LTD characteristics to optimize weight updates for accurate model derivation. After determining the blur kernel parameters, these values are input into an inverse convolution algorithm to recover the original image with high fidelity.

Supporting Information

Supporting Information is available from the Wiley Online Library or from the author.

Acknowledgements

Z.L. and M.H.J. contributed equally to this work. This research was supported by the NSFC Program (Grant nos. 62122055, 62104154, 62074104, 61974093, 62304137, and 52373248); by the Guangdong Provincial Department of Science and Technology (Grant nos. 2024B1515040002, 2021A1515012569, 2024A1515010006, and 2024A1515011718); by the Science and Technology Innovation Commission of Shenzhen (Grant nos. JCYJ20230808105900001, JCYJ20210324095207020, RCYX20200714114524157, JCYJ20220818100206013, JCYJ20220531102214032, 20231123155543001, and 20200804172625001). W.-Y.W. acknowledges the financial support from the Hong Kong Research Grants Council (PolyU 15307321), RGC Senior Research Fellowship Scheme (SRFS2021-5S01), Research Institute for Smart Energy (CDAQ), Research Centre for Nanoscience and Nanotechnology (CE2H), Research Center for Organic Electronics (CEOP) and Ms. Clarea Au for the Endowed Professorship in Energy (847S). M.Z. acknowledges the financial support from the National Natural Science Foundation of China (62205276), Research Centre for Organic Electronics (1-CE32), and the Hong Kong Research Grants Council (PolyU 15308324).

Conflict of Interest

The authors declare no conflict of interest.

Data Availability Statement

The data that support the findings of this study are available from the corresponding author upon reasonable request.

Keywords

charge transfer, image deblurring, polymeric memristors, synaptic plasticity, temperature-resilient resistive switching

Received: December 11, 2024
Revised: January 5, 2025
Published online: January 24, 2025

[1] R. Cao, X. Zhang, S. Liu, J. Lu, Y. Wang, H. Jiang, Y. Yang, Y. Sun, W. Wei, J. Wang, H. Xu, Q. Li, Q. Liu, *Nat. Commun.* **2022**, *13*, 7018.
[2] F. Li, D. Li, C. Wang, G. Liu, R. Wang, H. Ren, Y. Tang, Y. Wang, Y. Chen, K. Liang, Q. Huang, M. Sawan, M. Qiu, H. Wang, B. Zhu, *Nat. Commun.* **2024**, *15*, 3689.
[3] X. Pan, J. Shi, P. Wang, S. Wang, C. Pan, W. Yu, B. Cheng, S.-J. Liang, F. Miao, *Sci. Adv.* **2023**, *9*, eadi4083.
[4] X. Yu, C. Cheng, J. Liang, M. Wang, B. Huang, Z. Wang, L. Li, *Adv. Funct. Mater.* **2024**, *34*, 2312481.
[5] H. Zhang, H. Li, Y. Li, *Nano Lett.* **2024**, *24*, 4002.
[6] H. Zhao, Z. Liu, J. Tang, B. Gao, Q. Qin, J. Li, Y. Zhou, P. Yao, Y. Xi, Y. Lin, H. Qian, H. Wu, *Nat. Commun.* **2023**, *14*, 2276.
[7] G. Liu, Z. Lv, S. Batool, M. Z. Li, P. F. Zhao, L. C. Guo, Y. Wang, Y. Zhou, S.-T. Han, *Small* **2023**, *19*, 2207879.
[8] Z. Lv, S. R. Zhu, Y. Wang, Y. Ren, M. Luo, H. Wang, G. Zhang, Y. Zhai, S. Zhao, Y. Zhou, M.-H. Jiang, Y.-B. Leng, S.-T. Han, *Adv. Mater.* **2024**, *36*, 2405145.
[9] B. Zhang, W. Chen, J. Zeng, F. Fan, J. Gu, X. Chen, L. Yan, G. Xie, S. Liu, Q. Yan, S. J. Baik, Z.-G. Zhang, W. Chen, J. Hou, M. E. El-Khouly, Z. Zhang, G. Liu, Y. Chen, *Nat. Commun.* **2021**, *12*, 1984 .
[10] Z. Wang, L. Wang, Y. Wu, L. Bian, M. Nagai, R. Jv, L. Xie, H. Ling, Q. Li, H. Bian, M. Yi, N. Shi, X. Liu, W. Huang, *Adv. Mater.* **2021**, *33*, 2104370.
[11] Y.-B. Leng, Z. Lv, S. Huang, P. Xie, H.-X. Li, S. Zhu, T. Sun, Y. Zhou, Y. Zhai, Q. Li, G. Ding, Y. Zhou, S.-T. Han, *Adv. Mater.* **2024**, *36*, 2411225.
[12] J. Shi, Y. Lin, Z. Wang, X. Shan, Y. Tao, X. Zhao, H. Xu, Y. Liu, *Adv. Mater.* **2024**, *36*, 2314156.
[13] Z. Lv, Y. Wang, J. Chen, J. Wang, Y. Zhou, S.-T. Han, *Chem. Rev.* **2020**, *120*, 3941.
[14] C. Jiang, J. Liu, Y. Ni, S. Qu, L. Liu, Y. Li, L. Yang, W. Xu, *Nat. Commun.* **2023**, *14*, 1344.
[15] X. Zhang, H. Yu, W. Li, Y. Chen, N. Zeng, W. Shi, H. Ling, W. Huang, M. Yi, *ACS Appl. Mater. Interfaces* **2024**, *16*, 46527.
[16] D. B. Strukov, G. S. Snider, D. R. Stewart, R. S. Williams, *Nature* **2008**, *453*, 80.
[17] J. Li, Y. Qian, W. Li, S. Yu, Y. Ke, H. Qian, Y.-H. Lin, C.-H. Hou, J.-J. Shyue, J. Zhou, Y. Chen, J. Xu, J. Zhu, M. Yi, W. Huang, *Adv. Mater.* **2023**, *35*, 2209728.
[18] W. Chen, A. Chen, X. Liu, F. Shu, J. Zeng, J. Zhang, H. Xu, G. Peng, Z. Yang, J. Li, G. Liu, *Adv. Mater.* **2024**, *36*, 2410097.
[19] S. Liu, J. Zeng, Z. Wu, H. Hu, A. Xu, X. Huang, W. Chen, Q. Chen, Z. Yu, Y. Zhao, R. Wang, T. Han, C. Li, P. Gao, H. Kim, S. J. Baik, R. Zhang, Z. Zhang, P. Zhou, G. Liu, *Nat. Commun.* **2023**, *14*, 7655.
[20] H. Zhang, B. Jiang, C. Cheng, B. Huang, H. Zhang, R. Chen, J. Xu, Y. Huang, H. Chen, W. Pei, Y. Chai, F. Zhou, *Nano Lett.* **2023**, *23*, 3107.
[21] J. Lao, W. Xu, C. Jiang, N. Zhong, B. Tian, H. Lin, C. Luo, J. Travas-Sejdic, H. Peng, C. G. Duan, *Adv. Electron. Mater.* **2021**, *7*, 2100291.
[22] Y. Wang, Y. Gong, L. Yang, Z. Xiong, Z. Lv, X. Xing, Y. Zhou, B. Zhang, C. Su, Q. Liao, S.-T. Han, *Adv. Funct. Mater.* **2021**, *31*, 2100144.
[23] X. Shan, Z. Wang, J. Xie, J. Han, Y. Tao, Y. Lin, X. Zhao, D. Ielmini, Y. Liu, H. Xu, *Adv. Sci.* **2024**, *11*, 2405160.
[24] Z. Zhang, X. Zhao, X. Zhang, X. Hou, X. Ma, S. Tang, Y. Zhang, G. Xu, Q. Liu, S. Long, *Nat. Commun.* **2022**, *13*, 6590.
[25] Q. Zhang, D. Wu, Y. Fu, J. Li, Y. Chen, B. Zhang, *ACS Appl. Mater. Interfaces* **2024**, *16*, 22217.
[26] G. Zhou, J. Li, Q. Song, L. Wang, Z. Ren, B. Sun, X. Hu, W. Wang, G. Xu, X. Chen, L. Cheng, F. Zhou, S. Duan, *Nat. Commun.* **2023**, *14*, 8489.
[27] W. J. Ma, S. P. Lin, J. M. Luo, X. Y. Zhang, Y. Wang, Z. X. Li, B. Wang, Y. Zheng, *Appl. Phys. Lett.* **2013**, *103*, 262903.
[28] P. M. Sheridan, F. Cai, C. Du, W. Ma, Z. Zhang, W. D. Lu, *Nat. Nanotechnol.* **2017**, *12*, 784.
[29] K. Sun, Q. Wang, L. Zhou, J. Wang, J. Chang, R. Guo, B. K. Tay, X. Yan, *Sci. China Mater.* **2023**, *66*, 2013.
[30] S. J. Kim, I. H. Im, J. H. Baek, S. H. Park, J. Y. Kim, J. J. Yang, H. W. Jang, *ACS Nano* **2024**, *18*, 28131.
[31] Y. Song, G. Feng, L. Wu, E. Zhang, C. Sun, D. Fa, Q. Liang, S. Lei, X. Yu, W. Hu, *J. Mater. Chem. C* **2022**, *10*, 2631.
[32] L. Yin, R. Cheng, S. Pan, W. Xiong, S. Chang, B. Zhai, Y. Wen, Y. Cai, Y. Guo, M. G. Sendeku, J. Jiang, W. Liao, Z. Wang, J. He, *Adv. Mater.* **2023**, *35*, 2306850.
[33] I. Boybat, M. L. e. Gallo, S. R. Nandakumar, T. Moraitis, T. Parnell, T. Tuma, B. Rajendran, Y. Leblebici, A. Sebastian, E. Eleftheriou, *Nat. Commun.* **2018**, *9*, 2514.
[34] S. G. Sarwat, B. Kersting, T. Moraitis, V. P. Jonnalagadda, A. Sebastian, *Nat. Nanotechnol.* **2022**, *17*, 507.
[35] Y. Zheng, X. Guo, J. Jiang, Y. Fu, Q. Wang, D. He, *Appl. Phys. Lett.* **2024**, *125*, 083506.
[36] K. Gao, B. Sun, Z. Cao, X. Duan, W. Yan, G. Tong, G. Zhou, X. Chen, J. Shao, *Adv. Funct. Mater.* **2024**, *34*, 2401132.
[37] Q. Liao, Y. Wang, Z. Lv, Z. Xiong, J. Chen, G. P. Wang, S.-T. Han, Y. Zhou, *Org. Electron.* **2021**, *90*, 106062.
[38] X. Luo, J. Ming, J. Gao, J. Zhuang, J. Fu, Z. Ren, H. Ling, L. Xie, *Front. Neurosci.* **2022**, *16*, 1016026.
[39] X. Yan, J. Niu, Z. Fang, J. Xu, C. Chen, Y. Zhang, Y. Sun, L. Tong, J. Sun, S. Yin, Y. Shao, S. Sun, J. Zhao, M. Lanza, T. Ren, J. Chen, P. Zhou, *Mater. Today* **2024**, *80*, 365.
[40] K.-T. Chen, P.-L. Lin, Y.-C. Huang, S.-M. Chen, Z.-S. Liao, J.-S. Chen, *Adv. Funct. Mater.* **2025**, *35*, 2412452.
[41] Y. Cheng, Z. Li, Y. Lin, Z. Wang, X. Shan, Y. Tao, X. Zhao, H. Xu, Y. Liu, *Adv. Funct. Mater.* **2024**, *35*, 2414404.
[42] D. Ju, S. Kim, *Adv. Funct. Mater.* **2024**, *34*, 2409436.
[43] X. Zhang, Y. Zhuo, Q. Luo, Z. Wu, R. Midya, Z. Wang, W. Song, R. Wang, N. K. Upadhyay, Y. Fang, F. Kiani, M. Rao, Y. Yang, Q. Xia, Q. Liu, M. Liu, J. J. Yang, *Nat. Commun.* **2020**, *11*, 51.
[44] R. Yuan, P. J. Tiw, L. Cai, Z. Yang, C. Liu, T. Zhang, C. Ge, R. Huang, Y. Yang, *Nat. Commun.* **2023**, *14*, 3695.
[45] T. Wang, Z. Cui, Y. Liu, D. Lu, M. Wang, C. Wan, W. R. Leow, C. Wang, L. Pan, X. Cao, Y. Huang, Z. Liu, A. I. Y. Tok, X. Chen, *Adv. Mater.* **2022**, *34*, 2106212.
[46] G. Zhou, B. Sun, X. Hu, L. Sun, Z. Zou, B. Xiao, W. Qiu, B. Wu, J. Li, J. Han, L. Liao, C. Xu, G. Xiao, L. Xiao, J. Cheng, S. Zheng, L. Wang, Q. Song, S. Duan, *Adv. Sci.* **2021**, *8*, 2003765.
[47] Z. Liu, P. Cheng, R. Kang, J. Zhou, X. Zhao, J. Zhao, Z. Zuo, *Adv. Mater. Interfaces* **2022**, *10*, 2201513.
[48] F. Wan, Q. Wang, T. Harumoto, T. Gao, K. Ando, Y. Nakamura, J. Shi, *Adv. Funct. Mater.* **2020**, *30*, 2007101.
[49] G. Zhang, J. Qin, Y. Zhang, G. Gong, Z. Y. Xiong, X. Ma, Z. Lv, Y. Zhou, S.-T. Han, *Adv. Funct. Mater.* **2023**, *33*, 2302929.
[50] L. Zou, Z. Peng, H. Sun, Y. Yi, C. Zhu, J. Xu, J. Zhang, X. Hu, Y. Dang, L. Ye, X. Miao, *Adv. Funct. Mater.* **2024**, *35*, 2416325.
[51] J. Fu, J.-Y. Liu, G.-H. Zhang, Q.-H. Zhu, S.-L. Wang, S. Qin, L. He, G.-H. Tao, *Small* **2023**, *19*, 2302570.
[52] J. H. Yoon, M.-K. Song, W. Ham, K. J. Park, J.-M. Park, S. D. Namgung, J.-Y. Kwon, *Adv. Funct. Mater.* **2024**, *35*, 2415222.
[53] T. Zhang, L. Wang, W. Ding, Y. Zhu, H. Qian, J. Zhou, Y. Chen, J. Li, W. Li, L. Huang, C. Song, M. Yi, W. Huang, *Adv. Mater.* **2023**, *35*, 2302863.
[54] S. Liu, X. Zhong, Y. Li, B. Guo, Z. He, Z. Wu, S. Liu, Y. Guo, X. Shi, W. Chen, H. Duan, J. Zeng, G. Liu, *Adv. Sci.* **2024**, *11*, 2401080.
[55] Q. Zhang, Q. Che, D. Wu, Y. Zhao, Y. Chen, F. Xuan, B. Zhang, *Angew. Chem., Int. Ed.* **2024**, *63*, 202413311.
[56] S. Goswami, D. Deb, A. Tempez, M. Chaigneau, S. P. Rath, M. Lal, Ariando, R. S. Williams, S. Goswami, T. Venkatesan, *Adv. Mater.* **2020**, *32*, 2004370.
[57] B. Zhang, F. Fan, W. Xue, G. Liu, Y. Fu, X. Zhuang, X.-H. Xu, J. Gu, R.-W. Li, Y. Chen, *Nat. Commun.* **2019**, *10*, 736.

[58] Z. Zhao, M. E. El-Khouly, Q. Che, F. Sun, B. Zhang, H. He, Y. Chen, *Angew. Chem., Int. Ed.* **2023**, *62*, 202217249.
[59] Y. Guo, C. Yang, S. Zhou, Z. Liu, X. Guo, *Adv. Mater.* **2022**, *34*, 2204827.
[60] S. Wang, X. Dong, Y. Xiong, J. Sha, Y. Cao, Y. Wu, W. Li, Y. Yin, Y. Wang, *Adv. Electron. Mater.* **2021**, *7*, 2100014.
[61] X. Wen, W. Tang, Z. Lin, X. Peng, Z. Tang, L. Hou, *Appl. Phys. Lett.* **2023**, *122*, 173301.
[62] Z. He, X. Chen, H. Yu, Y. Du, M. Gao, S. Wang, C. Wang, *Chem. Eng. J.* **2023**, *457*, 141365.
[63] C. Wang, G. Liu, Y. Chen, R.-W. Li, W. Zhang, L. Wang, B. Zhang, *J. Mater. Chem. C.* **2015**, *3*, 664.
[64] S. Goswami, R. Pramanick, A. Patra, S. P. Rath, M. Foltin, A. Ariando, D. Thompson, T. Venkatesan, S. Goswami, R. S. Williams, *Nature* **2021**, *597*, 51.
[65] Z. Xu, Y. Li, Y. Xia, C. Shi, S. Chen, C. Ma, C. Zhang, Y. Li, *Adv. Funct. Mater.* **2024**, *34*, 2312658.
[66] L. Yuan, S. Liu, W. Chen, F. Fan, G. Liu, *Adv. Electron. Mater.* **2021**, *7*, 2100432.
[67] C. Zhang, C. Wang, C. Li, T. Zhang, Y. Jiang, X. Cheng, K. Wang, C. Ma, Y. Li, *Appl. Phys. Rev.* **2024**, *11*, 031303.
[68] V. W.-W. Yam, A. K.-W. Chan, E. Y.-H. Hong, *Nat. Rev. Chem.* **2020**, *4*, 528.
[69] C. Du, F. Cai, M. A. Zidan, W. Ma, S. H. Lee, W. D. Lu, *Nat. Commun.* **2017**, *8*, 2204.
[70] M. Lian, C. Gao, Z. Lin, L. Shan, C. Chen, Y. Zou, E. Cheng, C. Liu, T. Guo, W. Chen, H. Chen, *Light: Sci. Appl.* **2024**, *13*, 179.
[71] L. Sun, Z. Wang, J. Jiang, Y. Kim, B. Joo, S. Zheng, S. Lee, W. J. Yu, B.-S. Kong, H. Yang, *Sci. Adv.* **2021**, *7*, eabg1455.